CEAS Aeronautical Journal (2021) 12:441–456
https://doi.org/10.1007/s13272-021-00510-0

ORIGINAL PAPER

HLFC-optimized retrofit aircraft design of a medium-range reference configuration within the AVACON project

Tim Effing[1] · Florian Schültke[1] · Eike Stumpf[1]

Received: 3 June 2020 / Revised: 3 November 2020 / Accepted: 31 March 2021 / Published online: 18 April 2021

Abstract
This paper presents an approach for the design of a retrofit aircraft with integrated, optimized hybrid laminar flow control (HLFC). The basis for this research is a medium-range reference configuration derived within the German LuFo project "Advanced Aircraft Concepts" (AVACON). For the aerodynamics, an in-house-developed process chain for flow analysis is used, which requires airfoil shapes at specific sections of a known wing geometry. To improve the accuracy, pressure distributions from the 2D flow solver MSES are first aligned to high-fidelity 3D results from DLR's TAU code for extracted airfoils. This is done by varying parameters of the transformation methods used. Subsequently, the required suction distributions are optimized based on pre-defined criteria; these include not only the aerodynamic effects but also the needed mass flows. After optimizing the HLFC system architecture concerning mass and power offtakes, a retrofit aircraft is designed with the in-house "Multidisciplinary Integrated Aircraft Design and Optimization" (MICADO) environment. Compared to the turbulent baseline, the promising potential of the HLFC technology is demonstrated. In addition, the actual benefit of the optimization approach is evaluated in the context of overall preliminary aircraft design. This is done by redesigning the aircraft with other suction distributions and HLFC system architectures. Although it is shown that the approach leads to an overall optimum, the optimization benefit remains small. This indicates the limits of the HLFC technology as a pure add-on for initially turbulent aircraft and the need for the application of new laminar wing design methods to tap the full potential of HLFC.

Keywords Hybrid laminar flow control · Preliminary aircraft design · MICADO · Transformations methods

1 Introduction

The global aviation industry faces major challenges in terms of competitiveness, performance, and sustainability due to increasing globalization and public awareness. The resulting requirements for both manufacturers and operators can be derived from the well-known efficiency and sustainability goals for aviation (e.g., from the Flightpath 2050 [9]). Meeting such environmental aspects is key in the development of future aircraft. For this reason, several innovative technologies are currently investigated in the German LuFo project AVACON. One of these technologies is hybrid laminar flow control, whose potential has been repeatedly highlighted over decades as one of the most promising in terms of drag reduction for conventional aircraft [15, 20, 23, 28]. This expectation originates from the significantly reduced viscous drag of potential HLFC surfaces, which account for almost 30% of total drag in cruise [33].

1.1 Problem and approach

In AVACON, one of the major objectives is the investigation of different engine positions and their influence on overall aircraft design (OAD) level; due to the strong interaction between the wing and the engine, the detailed design of the wing is, therefore, mainly driven by the investigated engine position. To investigate the HLFC technology on the one hand and to not change the high fidelity design of the wing on the other hand, it was decided to create a retrofit design, i.e., analyze the potential of HLFC as an add-on for the initial wing. Even though a constant wing and airfoil geometry

✉ Tim Effing
effing@ilr.rwth-aachen.de

Eike Stumpf
stumpf@ilr.rwth-aachen.de

[1] Institute of Aerospace Systems (ILR), RWTH Aachen University, Wuellnerstr. 7, 52062 Aachen, Germany

limits the possible parameter space, an approach for optimizing the retrofit design in terms of suction distributions and HLFC system topology is established. The final benefit of this optimization is then examined at OAD level in terms of blockfuel (BF) consumption on a reference operating mission. To ensure high aerodynamic accuracy, synergies within the AVACON project are used; this is done by comparing and consequently adjusting results from a 2D flow solver to 3D results; the latter have been kindly provided by the project partners from the Institute of Aerodynamics and Flow Technology of the German Aerospace Center (DLR-AS). Thus, this work is divided into three parts:

1. Alignment of pressure distributions (Sect. 3);
2. Optimization of retrofit aircraft (Sect. 4);
3. Examination of actual benefit (Sect. 5).

The necessary fundamentals for these three parts are presented in the next section.

2 Fundamentals

Regardless of the different engine positions, a backward swept wing is used for all aircraft configurations in AVACON. With regard to flow laminarization on this wing geometry, different critical instability mechanisms must be considered:

- Tollmien–Schlichting instability (TSI).
- Cross-flow instability (CFI).
- Attachment-line transition (ALT).

The two-dimensional Tollmien–Schlichting waves mostly occur behind the maximum thickness of an airfoil due to their amplification by positive pressure gradients. The three-dimensional cross-flow instabilities, however, occur with increasing sweep angles due to the additional pressure gradient along the wingspan and the associated three-dimensionality of the boundary layer. In contrast to TSI, cross-flow instabilities mostly occur in regions close to the leading edge as they are destabilized by negative pressure gradients [29]. The third instability mechanism (ALT) can cause a transition right at the attachment line of the flow. For further information about ALT, the reader may refer, for example, to Refs. [22, 24]. A promising approach for simultaneously addressing all critical instability mechanisms is hybrid laminar flow control (HLFC); this technique combines the shaping of the airfoil in the mid-chord region (natural laminar flow, NLF) with the application of active suction ahead of the front spar (laminar flow control, LFC) [15]. Most recently, the potential of a simplified HLFC system on the vertical tailplane of an Airbus A320 was demonstrated in a flight test [30].

For this work, it is important to emphasize that the use of an HLFC system as a pure add-on prevents the favorable shaping of the geometry. This is why the optimization approach concentrates on the LFC part; however, the characteristic HLFC boundary for suction just ahead of the front spar is maintained.

To analyze the critical instability mechanisms, a so-called quasi-three-dimensional (2.5D) approach developed at the Institute of Aerospace Systems (ILR) at RWTH Aachen University is used. This approach is based on an iterative process coupling the 2D flow solver MSES [6] with the 3D transition prediction module STABTOOL [31, 32] through transformation rules for flow conditions and wing geometry. Since the relations between 2D and 3D flow characteristics are of special interest in Sect. 3 and the 2.5D approach is used for the aerodynamics in Sects. 4 and 5, a short, but not exhaustive overview is given below. In addition, the general approach for the design of an aircraft with integrated hybrid laminar flow control with MICADO is briefly described. For detailed information about the approach, the reader may refer to Risse [27].

2.1 Transformation rules between 2D and 3D

To consider aerodynamic characteristics of a 3D swept wing geometry within the 2.5D method, equivalent characteristics of 2D airfoil sections must be derived. For infinite swept wings, the so-called simple sweep theory (SST) has been established by Busemann [4]. For the 2D application case, the SST recommends transforming a 3D Mach number Ma_{3D} with the cosine of a reference angle φ_{ref}. For swept wing geometries, it was shown, e.g., by Boppe [3] that the local sweep angle at the shock position provides reasonable results for SST conversions. Likewise, the 3D lift coefficient can be transformed as a function of φ_{ref}. Due to the conversion to 2D, the influence of cross-flows must be additionally considered; therefore, the SST is extended by a non-dimensional parameter "x", which results in the following equations:

$$\mathrm{Ma}_{2\mathrm{D}} = \mathrm{Ma}_{3\mathrm{D}} \cdot \cos^{x}(\varphi_{\mathrm{ref}}), \tag{1}$$

$$C_{\mathrm{l,2D}} = \frac{C_{\mathrm{l,3D}}}{\cos^{2x}(\varphi_{\mathrm{ref}})}. \tag{2}$$

This exponent "x" ranges from "0" (no transformation) to "1" (infinite swept wing). Although various values have been proposed, e.g., by Anderson [1] or Torenbeek [39], there is no clear definition; this allows parameter variations to reproduce cross-flow effects when the real effects are accurately known in advance. A similar approach has already been conducted by Schültke [36] for different wing geometries. The default value used within the 2.5D approach is the value for infinite swept wings.

In addition to the freestream conditions, the airfoil needs to be transformed. For this, there are different methods to create 2D airfoil geometries, such as transformations in line of flight or perpendicular to a reference line of the wing. The transformation method used within this work follows the conical-flow concept, i.e., transformation is done perpendicular to a conical arc chord [38]. For further information, the reader is referred to Risse [27].

Whereas the transformation rules mentioned above enable the use of the 2D flow solver MSES, the resulting pressure distribution needs to be transformed to 3D to predict the transition position with the 3D program suite STABTOOL. Under the assumption of conical flow, i.e., the isobars follow a constant relative chord-wise position, Lock's equivalence law is used. This method establishes a relation between 2D and 3D pressure coefficients [17]:

$$C_{p,3\mathrm{D}} = \frac{2(f-1)}{\kappa \cdot \mathrm{Ma}_{3\mathrm{D}}^2} + f \cdot C_{p,2\mathrm{D}} \cdot \cos^{2x}\left(\varphi_{\mathrm{ref}}\right). \tag{3}$$

Besides the ratio of the specific heat of air (κ), the local sweep angle of the respective relative chord-wise position $\varphi_{x/c}$, as well as a specific factor f, is used; the latter is defined by

$$f = \left[\frac{2 + (\kappa-1)\cdot \mathrm{Ma}_{3D}^2 \cdot \cos^2\left(\varphi_{x/c}\right)}{2 + (\kappa-1)\cdot \mathrm{Ma}_{3D}^2 \cdot \cos^{2x}\left(\varphi_{\mathrm{ref}}\right)}\right]^{\frac{\kappa}{\kappa-1}}. \tag{4}$$

Next, the 2.5D approach, which uses all the transformation rules described above, is briefly introduced.

2.2 Quasi-three-dimensional approach

The 2.5D process chain starts with calculating the flow around 2D airfoils at specific wing sections, taking into account 3D freestream conditions, 3D lift coefficients, and transition points. Both the freestream conditions and the lift coefficients are transformed to 2D using Eqs. (1–2). Additionally, an automatic shock detection is implemented by identifying the exceeding of local maximum values of the density gradient. The outputs are not only 2D pressure distributions but also viscous and wave drag coefficients. After transforming the 2D pressure distribution to 3D using Lock's method, the transition point is calculated within the physics-based program suite STABTOOL. This is done by analyzing the boundary layer for the given 3D pressure data and preset suction distributions. While STABTOOL focuses on TSI and CFI, ALT is evaluated quantitatively using the so-called Pfenninger–Poll criterion, which was derived from wind-tunnel tests conducted at ONERA [25].[1] The resulting transition point is then fed back into MSES as an updated input variable. After convergence is achieved, a single execution of the method provides both the viscous and the wave drag coefficients of a 2D airfoil while also taking the transition position into account.

Since the variation of the suction distribution is part of the optimization approach in Sect. 4, the effects of different suction shapes will be briefly discussed.

2.3 Effects of different suction distributions

To determine the transition point with the 2.5D method, a suction distribution must be specified by the user. This distribution is parameterized and can, therefore, take various forms; four different suction types, which follow mathematical functions and have been implemented in the method, are exemplary shown in Fig. 1.

The suction is described with its strength $C_{\mathrm{q}} = w/u_{\infty}$, expressing the suction velocity $w \leq 0$ as a fraction of the freestream velocity u_{∞}, and its start- and endpoint $(x/c)_{\mathrm{suction,start/end}}$. It holds for all suction types that the maximum suction strength $C_{q,\max}$ is at the leading edge to prevent transition through highly amplified CFI. In addition, the suction length is limited by the front spar position of the respective wing section. The authors already pointed out that the different suction types can lead to identical aerodynamic results [8]. Nonetheless, further studies did not reveal specific aerodynamic advantages for any single distribution type. Since the suction shape in the upper left corner in Fig.1 has already been used, e.g., by Boeing for research purposes [10] and requires less complex installation on the wing, this suction type is selected for the further course of this research. It is divided into two sections: In the first section, the suction strength decreases linearly. In the second section, the suction strength keeps a constant level up to the endpoint. Previous studies have already shown that in addition to $C_{q,\max}$, the suction length, represented by the relative endpoint of the suction area $(x/c)_{\mathrm{suction,end}}$, has a significant influence on the transition position. In contrast, the starting

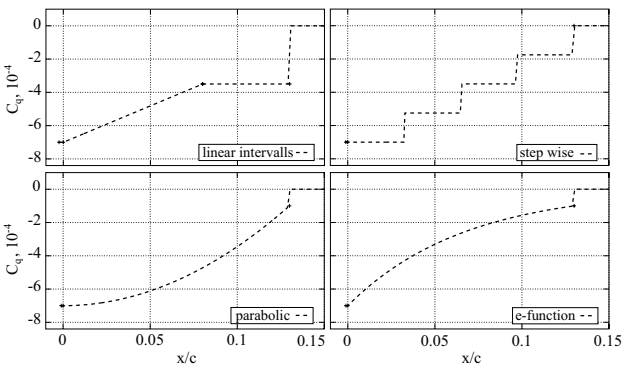

Fig. 1 Different suction distributions [8]

[1] In the course of this work, ALT will not be further considered. The criterion has been checked for all cases, however, and found to be noncritical; especially if it is assumed that the critical limit can be shifted using passive devices such as Gaster bumps [2].

point and start value of the second interval have a minor influence on the aerodynamic results [35].

Next, the integration of the 2.5D approach and the design of an HLFC system in MICADO are introduced.

2.4 HLFC aircraft design with MICADO

Preliminary overall aircraft design usually does not aim at the analysis of individual points but rather at the calculation of entire drag polars. Thus, numerous variations of both the Mach number and the 3D lift coefficient are inevitable. For this reason, turbulent and laminar drag polars are calculated with the 2.5D approach and pre-defined suction distributions for geometric key points; these include the inner and outer stations of every given wing segment. The data is then stored in an aerodynamic database, which can be accessed in the aerodynamics tool of MICADO during the aircraft design process. This is done using the local lift distribution calculated with the multiple lifting line code LIFTING_LINE [11, 13]. Whenever data are queried from a relative spanwise position that is not stored in the database, the available data of the inner and outer station of the respective wing segment are interpolated.

Besides the calculation of the aerodynamic performance, an HLFC system needs to be designed to evaluate aircraft with integrated hybrid laminar flow control. Therefore, an HLFC system design methodology has been implemented into the MICADO environment at the ILR; this methodology is generally based on the simplified suction concept, which originates from the European ALTTA project for the A320 fin [12]. This concept requires a perforated surface, suction chambers, and the integration of one or more compressors to guarantee the suction pressure for a specified suction distribution. These compressors need a certain amount of electrical power, which is usually provided by the electric generators of the aircraft. The resulting suction flow from the compressors is collected in one or more pipes and consequently led to the outside through an outflow valve at the wing–fuselage intersection. In general, the HLFC system with its components is sized with the amount of sucked air and the pressure difference to be overcome. For this concept, supplementary methods and equations proposed by Pe and Thielecke [18] are implemented in the HLFC system sizing methodology. The required input parameters include both pre-defined suction distributions as well as the pressure distributions for the design Mach number and design altitude of the HLFC system. The most important output parameters of this module are the total HLFC system mass ($m_{\mathrm{HLFC,tot}}$) and the total electrical power required to maintain the specified suction distributions ($P_{\mathrm{HLFC,tot}}$). The required system power depends only on the needed power for the compressors and the efficiency of both the motors and the variable frequency drive. The total system mass sums up the mass of all components.

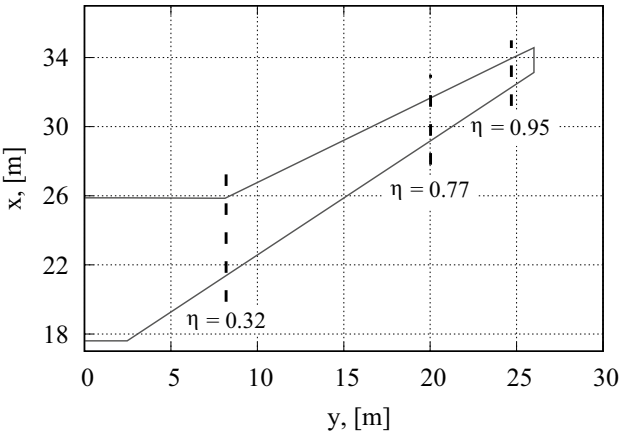

Fig. 2 Wing planform of ARB2028

This design methodology has some outstanding advantages for preliminary aircraft design, e.g., the fast and robust prediction of transonic (laminar) drag polars. These advantages have been successfully demonstrated by Risse [27], who conducted overall aircraft design studies with integrated HLFC technology using this approach. Nonetheless, accuracy losses must be expected due to the early design stage. For the 2.5D approach, in particular, Schültke [36] pointed out that deviations from high fidelity TAU results are unavoidable, especially for kinked wings. Hence, the pressure distributions from MSES are first compared to the ones extracted from TAU results from Lange [16] in the next section.

3 Alignment of pressure distributions

In this section, results from the 2D flow solver MSES are compared and subsequently aligned to results from the DLR-TAU code [37]. Since this research concentrates on HLFC wing integration, which promises the greatest savings potential due to the large wetted areas, the wing geometry of the AVACON Research Baseline 2028 (ARB2028)[2] is introduced first. Figure 2 shows the planform of the wing, which has a span of 52 m. In addition, characteristic slices of the outboard segment which are used in the following are highlighted with dashed lines.

The outboard (OB) segment, which is of special interest for the HLFC application, has a leading-edge sweep angle

[2] Although minor design changes were made during the project, the reader may refer to Ref. [42] for general information about the initial version of the ARB2028.

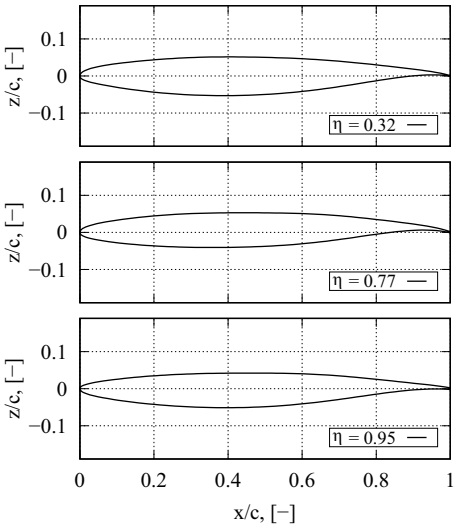

Fig. 3 Used airfoils in ARB2028 OB wing

of $\varphi_{LE} = 33.43°$ and a trailing-edge sweep angle of $\varphi_{TE} = 26.02°$, respectively. For the required 2D airfoil data, the 3D geometry originally set up by Lange [16] for the high-fidelity design is used; the airfoil sections used for this design are based on the well-known Common Research Model (CRM) [40]. To avoid the possible influence of the dihedral being transferred to the 2D calculation, the wing geometry is cut perpendicular to the surface at characteristic points (see dashed lines in Fig. 2). To ensure good further processing within the 2.5D method, the speed distributions of the extracted airfoils are consequently smoothed using the so-called Hanning window filter from XFOIL. For more information about the functionality of this filter function and XFOIL in general, the reader may, e.g., refer to Refs. [5, 7]. The resulting airfoil geometries of the OB segment are illustrated in Fig. 3.

The airfoils at the relative spanwise positions $\eta = 0.32$ with a maximum relative thickness of $(t/c)_{max} = 10.5\%$ and $\eta = 0.95$ with $(t/c)_{max} = 9.3\%$, respectively, mark the HLFC application area. The additional airfoil at $\eta = 0.77$ with $(t/c)_{max} = 9.4\%$ results from a significant change in the twist angle and thus a new characteristic wing segment [16].

The following comparison is conducted for the airfoils shown in Fig. 3 and their respective local $C_{l,3D}$-values at the global design point $C_L = 0.5$ and $Ma_{3D} = 0.83$. The input parameters for the last and thus converged MSES run are listed in Table 1.

It is obvious that the $C_{l,3D}$-values are transformed to higher $C_{l,2D}$-values using both the initial estimate of the transformation exponent "x" being equal to 1 (see Sect. 2.1) and the transformation angle resulting from the automatic shock detection (see Sect. 2.2). In Fig. 4, the results transformed to 3D from the converged run of the 2.5D method proposed by Risse [27] (solid line) as well as the respective TAU results (dashed line) are shown. For a detailed analysis of the 3D results, the reader is referred to Lange [16]; in this section, the focus is only on deviations between the two methods.

Table 1 MSES input parameters (converged run)

η	$C_{l,3D}$	φ_{ref}	Transf.-exponent x	$C_{l,2D}$
0.32	0.59	30.41°	1.00	0.79
0.77	0.65	29.99°	1.00	0.87
0.95	0.37	32.90°	1.00	0.53

It can be observed that the MSES results show deviations from the TAU results. For all three spanwise positions, the shock position is detected further upstream compared to the TAU results. This indicates that the transformation angle used as a result of the automatic shock detection is too large since the shock position moves forward with increasing transformation angle [36]. Also, when a shock is detected, MSES predicts that it is stronger than the corresponding counterpart in the TAU results. This, in turn, indicates that the initial estimate of the transformation exponent, which is used in Eqs. (1–4), being equal to "1" can be improved [36]. Despite the shock positions and strengths, especially the results at $\eta = 0.32$ and $\eta = 0.95$, respectively, reveal high deviations in the overall pressure distribution. This is mainly due to an increased influence of cross-flow velocities at the inboard wing segment and the wingtip. This assumption is supported by the results at $\eta = 0.77$ since there is a relatively good agreement with the 3D results except for the shock and a slightly increased suction peak at the leading edge. To achieve a higher aerodynamic accuracy within the overall design loop, the following steps are taken to approximate the results from MSES to the TAU results:

- The transformation angle is set to the local angle at the (most aft) shock position $(x/c)_{ref}$ from the known TAU results;
- Analogous to the approach proposed by Schültke [36], the transformation exponent "x" from Eqs. (1–4) is varied from 0.0 to 1.0 with a step size of 0.1.

This approach leads to several different MSES calculations from which the results with the best agreement are selected; the input parameters for the respective converged MSES runs are listed in Table 2.

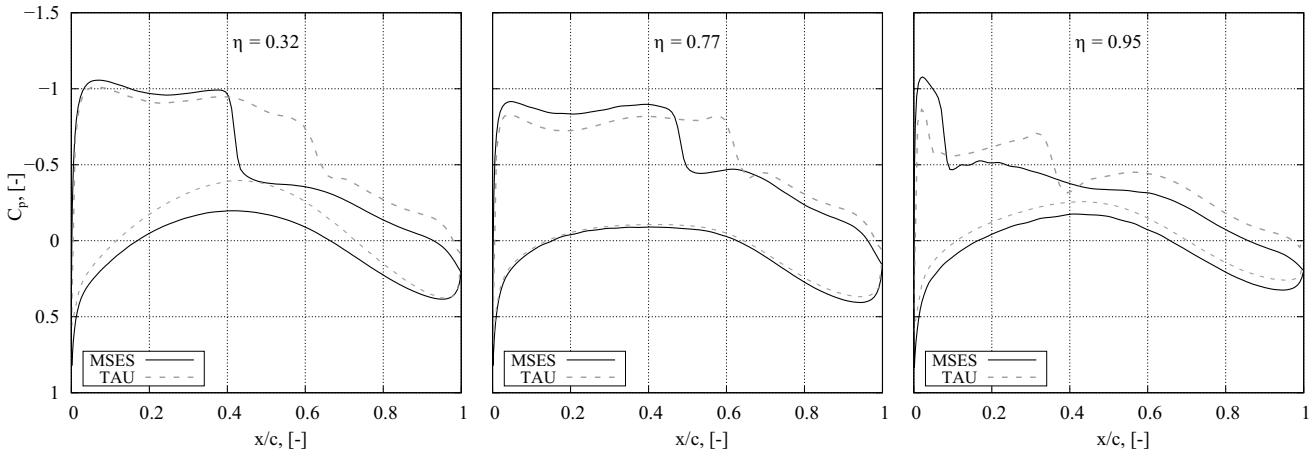

Fig. 4 Comparison of pressure distributions of MSES with TAU results at various stations of ARB2028 wing

Table 2 MSES input parameters (best candidates)

η	$C_{l,3D}$	φ_{ref}	Transf.-exponent x	$C_{l,2D}$
0.32	0.59	29.12°	0.65	0.70
0.77	0.65	29.12°	0.85	0.82
0.95	0.37	31.14°	0.65	0.45

Table 3 Final settings for 2.5D approach

η	$(x/c)_{ref}$	Exponent x
0.32	0.60	0.65
0.77	0.60	0.85
0.95	0.33	0.65

As expected, reduced transformation angles and exponents result in less deviations of the pressure distributions; the final 3D pressure distributions are shown in Fig. 5.

First, it can be seen that the pressure distributions in Fig. 5 show a better agreement, as previously in Fig. 4; this holds for all three relative spanwise positions. Nevertheless, it is obvious that, although important characteristics have been conveniently approximated, an exact match cannot be achieved. This again refers in particular to the kink and tip airfoils of the OB wing segment, which require a considerably high correction of cross-flow effects with a transformation parameter of $x = 0.65$. In contrast, for the section $\eta = 0.77$ at which the cross-flow effects are expected to be less, a transformation parameter of $x = 0.85$ is sufficient. These results comply with the findings from Schültke [36], who pointed out that especially the consideration of tip vortices is not possible with the method used.

The resulting settings are summarized in Table 3; in the following, these will be kept constant throughout the calculation of the (laminar) drag polars for the HLFC retrofit design.

In the next section, the derivation and optimization of the HLFC retrofit design will be presented.

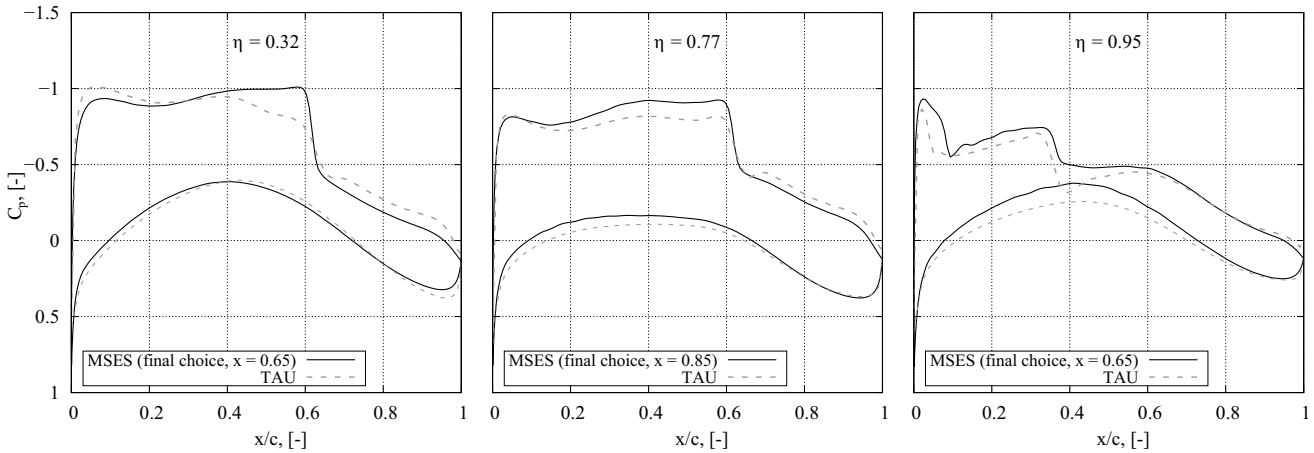

Fig. 5 MSES results with final choice of transformation parameter x compared to TAU results

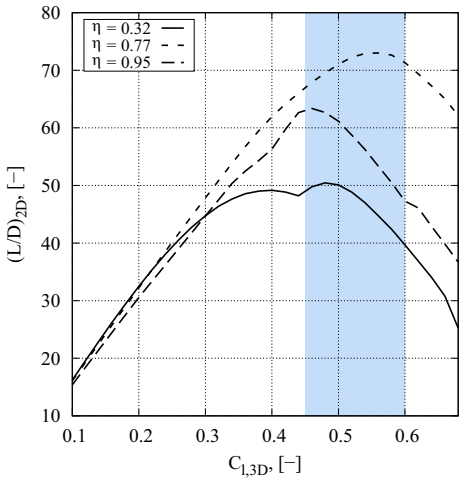

Fig. 6 Turbulent ARB2028 airfoil characteristics

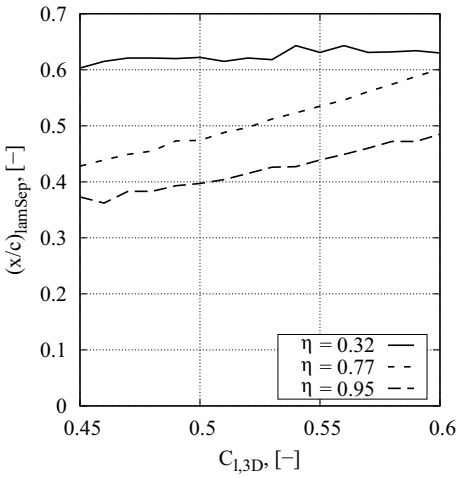

Fig. 7 Laminar potential of the ARB2028 OB wing

4 Optimization of retrofit aircraft

To estimate the potential of HLFC integration, an HLFC system is installed in the outboard wing of the ARB2028. Thus, not only the aerodynamics but also the system itself can be optimized. For the derivation of the optimized HLFC retrofit design, the following steps are conducted:

1. Identification of optimum suction distributions;
2. Optimization of the HLFC system architecture;
3. Derivation of optimized HLFC retrofit design.

Consequently, the optimization approach includes three steps, which will be discussed below.

4.1 Identification of optimum suction distributions

The identification of optimum suction distributions for the characteristic wing stations starts by analyzing the sectional turbulent characteristics of the affected airfoils from Fig. 3; this is done to get a first indication of the expected performance. For this, the aerodynamic performance in terms of lift-to-drag ratio (*L/D*) including viscous and wave drag in dependence of the lift coefficient $C_{l,3D}$ is calculated with the 2.5D approach and the settings listed in Table 3. The results are shown in Fig. 6.

The solid curve reflects the characteristics of the kink airfoil ($\eta = 0.32$), which shows its best performance for $Ma = 0.83$ at a lift coefficient of $C_l = 0.48$. The minor bump at $C_l = 0.44$ is caused by the fact that from $C_l = 0.46$ on, a previously detected second shock disappears; thus, the wave drag increases less with increasing lift coefficient. Despite that, compared with the outer stations, this airfoil shows weaker overall performance. One reason for this could be the over-prediction of shocks (see left side in Fig. 5), which results in an increased wave drag. It is evident that for turbulent flow conditions, the highest aerodynamic performance for all three investigated airfoils is achieved in the highlighted range of approximately $0.45 \leq C_l \leq 0.6$. For this range, a rough estimation of the laminar potential, which is represented by the laminar separation of the boundary layer[3] in relative chordwise position, can be derived from Fig. 7.

It is evident that the airfoils—although initially derived from the turbulent CRM—offer convenient laminar potential, which additionally rises with increasing C_l-values. Especially the airfoil at $\eta = 0.32$ has to be emphasized, because this station reveals satisfying laminar potential, although the turbulent characteristics show weak performance. The maximum potential for all stations ranges roughly between 50 and 60% of the local chord. These values can be considered as the expected boundaries for the laminar flow extension, i.e., even if the laminarization is fully optimized for every airfoil, the flow would turn into a turbulent flow after reaching the respective local chord positions.

Due to the high backward sweep of the ARB2028 wing with $\varphi_{LE} = 33.43°$, cross-flow instabilities are highly amplified. At this point, applying flow suction ahead of the front spar can suppress the amplification and extend the laminar area. Moreover, convenient suction also shifts the beginning of the destabilizing influence of Tollmien–Schlichting waves behind the endpoint of the suction area. Thus, the endpoint is set to 20% local chord, which marks a reasonable front spar position. Furthermore, the suction region is divided into two intervals at 10% local chord (see Sect. 2.3). Keeping the

[3] The boundary-layer equations are numerically solved within the STABTOOL module COCO [31] using Newton's method. The point of laminar separation is hereby defined as the point where no convergence is achieved even with increased grid fineness.

Table 4 Variation of suction distribution

Parameter	#	start value	end value	step size
$C_{q,start,sec1}$	1	0.0	$-1.6e^{-3}$	$-0.2e^{-3}$
$C_{q,start,sec2}/C_{q,start,sec1}$	2	0.0	1	0.1

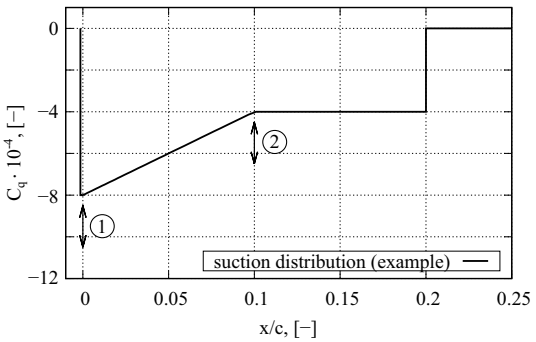

Fig. 8 Variation of suction distribution (example)

general shape constant, two parameters of the applied suction are varied, as stated in Table 4; this is done for every airfoil from Fig. 3. The start value of the second section is represented by a fraction of the start value of the first section ($C_{q,start,sec2}/C_{q,start,sec1}$). In addition, the parameter variations are exemplary shown in Fig. 8.

Besides $C_{q,start,sec1}$, which has a significant influence on the transition, also the start values of the second section are varied. Although the influence on the aerodynamics is expected to remain small (cf. Sect. 2.3), the required mass flows may influence the selection. The results of this study are presented in Fig. 9 as scatter plots due to the amount of available data. Lift-to-drag ratios corresponding to the different suction profiles are thereby represented by blue dots; in addition, two boundary curves for an upper and lower limit are given for the relative spanwise positions η =0.32 and $\eta = 0.77$, respectively. The findings for $\eta = 0.95$ are similar to the ones for $\eta = 0.77$ and are additionally shown in Fig. 23 in the Appendix.

Comparing the two figures, it becomes obvious that the aerodynamic performance at $\eta = 0.32$ is less promising than for the wing section at $\eta = 0.77$. This is mainly due to different airfoil geometries, influences of cross-flow velocities, and differences in shock strengths at constant $C_{l,3D}$-values. Nonetheless, a significant increase in the aerodynamic performance up to 38% is possible for $\eta = 0.32$ (left side in Fig. 9). In addition, it is evident that some suction distributions are not sufficient to dampen CFI, resulting in a direct transition to a fully turbulent flow close to the leading edge. For $\eta = 0.77$ (right side), however, a considerable increase in aerodynamic performance is revealed for all suction profiles. This also includes the suction distribution with a start

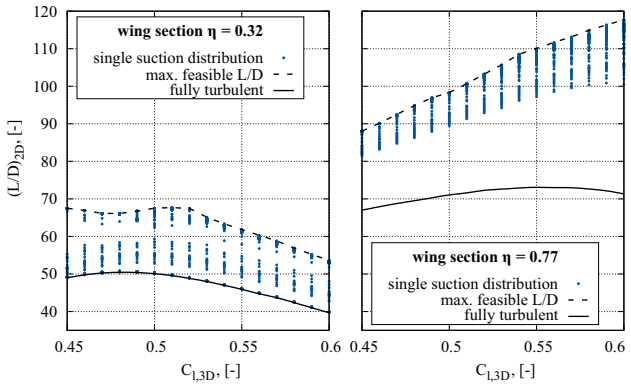

Fig. 9 Aerodynamic performance increase for different suction distributions (left: $\eta = 0.32$; right: $\eta = 0.77$)

and end value of $C_q = 0$ (no suction at all), indicating a favorable behavior of the pressure gradients for NLF application. For example, compared to the turbulent calculation at $C_{l,3D} = 0.55$, an increase of about 25% of aerodynamic performance is achieved even for the least beneficial laminar calculation. Nonetheless, the laminar performance can be further increased by applying active suction. Additionally, the difference between the performances of the single suction distributions spreads out with increasing local C_l -values; thus, the benefit of the applied suction becomes larger. But it also becomes clear that several suction distributions result in the same aerodynamic improvement. This implies that optimum suction distributions cannot be clearly identified solely on the basis of aerodynamic performance. For this reason, the required mass flow is taken as an additional criterion. The approach to identify an optimum suction distribution out of the data from the scatter plots is shown in Fig. 10.

This approach takes into account the aerodynamics already mentioned as well as the required mass flows; this is done for the whole C_l-range and, thus, for both the optimum and the off-design flight conditions. First of all, a range of possible candidates is determined based on the maximum possible *L/D*. This ensures that not only the suction distribution with the maximum *L/D* but also other candidates that come close to this value and may possibly require significantly less mass flow, are considered in the selection. Based on this, the candidate, which requires the lowest mean mass flow, is selected. In a last check, the off-design performance in terms of Reynolds number changes is checked; this excludes candidates who cannot prevent transition jumps caused by changes in the Reynolds number [8]. Finally, an unique suction distribution for every spanwise position analyzed is selected. The final, optimized suction distributions are illustrated in Fig. 11.

It becomes clear that the approach results in different values for $C_{q,start,sec1}$ and ($C_{q,start,sec2}/C_{q,start,sec1}$) for each airfoil.

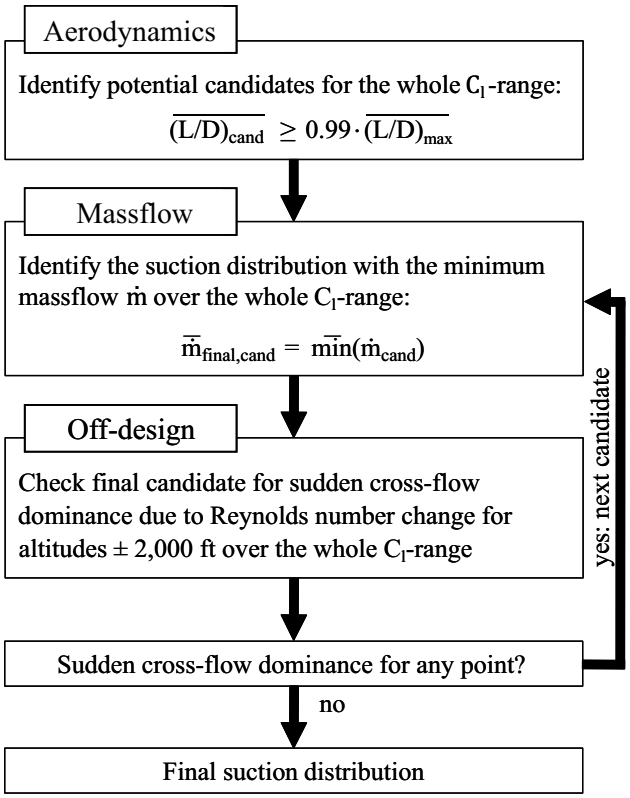

Fig. 10 Identification of optimum suction distributions

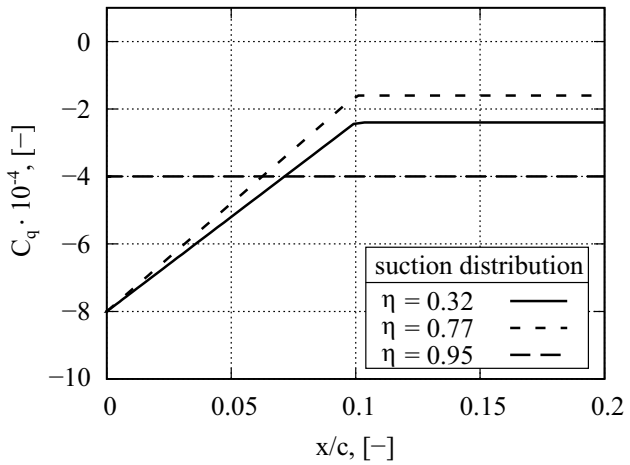

Fig. 11 Identified optimum suction distributions

To put the different suctions into perspective, it is noted that the influences of the Reynolds number as well as different airfoil geometries on the amplification of the relevant instability mechanisms have already been demonstrated by the authors in Ref. [8]. Since this amplification correlates directly with the required suction strength, both factors can have an influence.

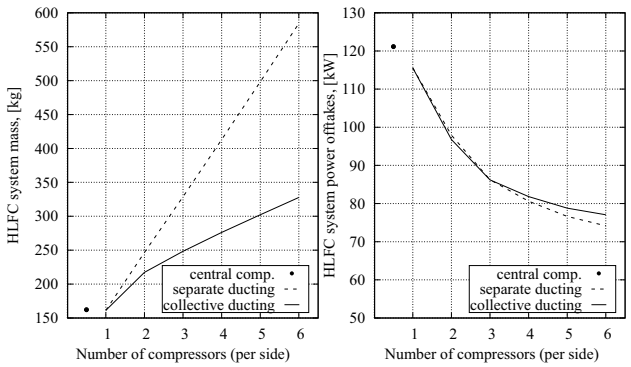

Fig. 12 Masses and power requirements for different HLFC system architectures

Based on these identified suction distributions, the next step is to optimize the HLFC system architecture.

4.2 Optimization of the HLFC system architecture

As described in Sect. 2.4, the HLFC system design method requires the Mach number and the altitude at which the HLFC system is operated. Thus, for the subsequent studies, the cruise Mach number of $Ma = 0.83$ and the initial cruise altitude of ICA = 35,000 ft is used.

For the ARB2028, different topology options can be investigated, such as a centralized architecture with one large compressor or a decentralized architecture with several smaller compressors. The latter additionally enables the adaption of the number of compressors distributed along the span. Moreover, the two different ducting architectures can be investigated: Either each compressor is connected to a separate duct or all compressors are connected to a collective one. To choose the most promising architecture for the ARB2028 wing, the different architectures are investigated for the identified suction distributions. This is done by comparing the overall system mass $m_{HLFC,tot}$ and power requirement $P_{HLFC,tot}$ related to the number of compressors. Similar topology studies using the design methodology presented in Sect. 2.4 have already been conducted in the German LuFo projects HIGHER-LE and VERS^{2}US. For further information, the reader may refer to Pe [19]. The results of this ARB2028 study are presented in Fig. 12.

The solid curves represent the architecture that uses only one collective duct, whereas, for the dashed curves, every compressor uses an own (separate) duct. In the left figure, the total HLFC system mass $m_{HLFC,tot}$ is increasing with the number of compressors. It is self-evident that the system mass is augmenting with additional ducts even if the cross section of each duct can be reduced. In terms of mass, a collective ducting system should be used. The comparison of the architectures in terms of total power requirements

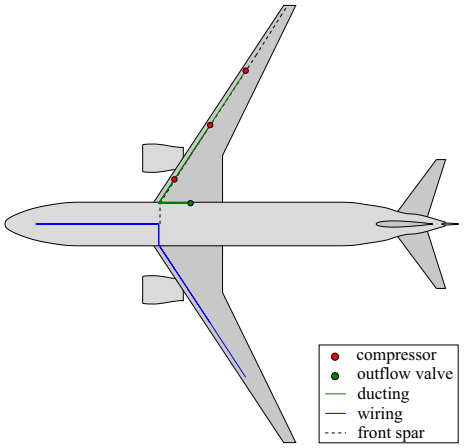

Fig. 13 Final HLFC system architecture

Table 5 Final key parameters of HLFC system

Parameter	Unit	Value
Number of compressors (per side)	–	3
$m_{\mathrm{HLFC,tot}}$	kg	≈ 248
$P_{\mathrm{HLFC,tot}}$	kW	≈ 86

$P_{\mathrm{HLFC,tot}}$ indicates no significant difference between the collective and the individual ducting (see right side in Fig. 12). With an increasing number of compressors, however, the power requirement decreases and almost converges from 3 compressors upwards. The power-saving with more than three compressors is disproportionate to the mass increase. That is why the final chosen configuration for the HLFC system is a decentralized architecture with three compressors and a collective ducting system. This architecture is depicted in Fig. 13.

The red dots mark the compressors, the green lines the ducting system with the outflow valve (green dot), and the blue line represents the electric wiring from the avionic bay to the compressors. The final parameters for the chosen HLFC system architecture can be found in Table 5.

With this architecture and the previously optimized suction distributions, the HLFC retrofit is derived next.

4.3 Derivation of optimized HLFC retrofit design

For a suitable starting point for the evaluation of the HLFC technology, a turbulent reference (TR) of the ARB2028 is designed using MICADO [26, 34] as well as the database approach (see Sect. 2.2). For the following results, the relevant key parameters of this trimmed TR are listed in Table 6.

Table 6 Relevant key parameters of turbulent reference

Parameter	Unit	Value
Max. take-off mass (MTOM)	t	≈ 140.2
Operating mass empty (OME)	t	≈ 81.0
$(L/D)_{\mathrm{opt}}$	–	≈ 20.2
BF design mission (4600 NM)	t	≈ 30.1
BF study mission (2000 NM)	t	≈ 13.2

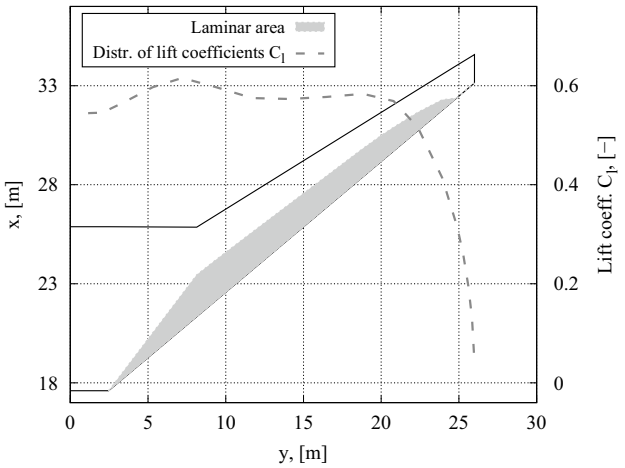

Fig. 14 Laminar area in cruise flight

One of the basic requirements for maintaining a laminar flow is the creation or maintenance of a smooth wing surface. Apart from constructional irregularities, contamination of the surface by rain, ice, sand, insects, or other particles in the air must be prevented during flight [44].[4] To enable the application of the HLFC technology, the slats used to this point are thus replaced by Krueger flaps. Besides the fact that it has already been shown that these high-lift devices can provide the required high-lift performance [14], Krueger flaps passively prevent the contamination mentioned above.

Starting with the aerodynamic benefit of the HLFC application, the laminar area for the optimum point in cruise flight calculated with the aerodynamics module of MICADO is shown in Fig. 14. In addition, the dashed curve shows the distribution of the local lift coefficients.

Figure 14 shows that the laminar surface at the wing-fuselage transition slowly builds up to the kink, and from there remains approx. constant at $(x/c)_{transition} \approx$ 50% over the entire application area. Taking into account

[4] Remaining uncertainties due to contamination under realistic operating conditions are not part of this study. Information about the operational and economic effects of contamination on the laminarity can, e.g., be found in Refs. [21, 41, 43].

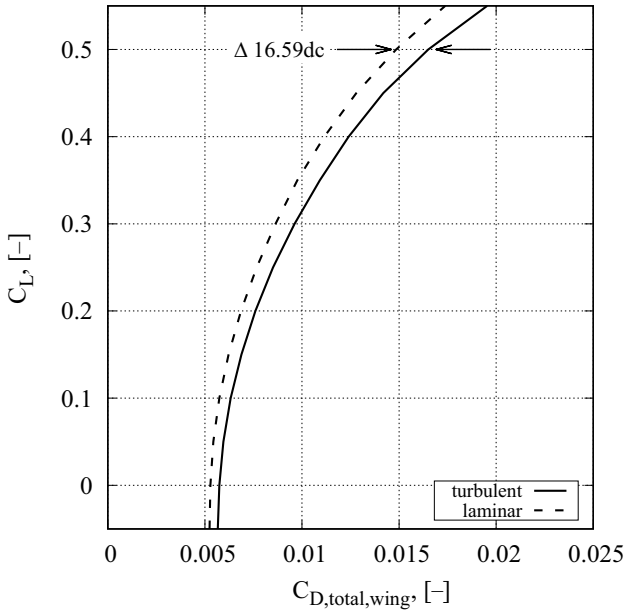

Fig. 15 Shift of wing polars

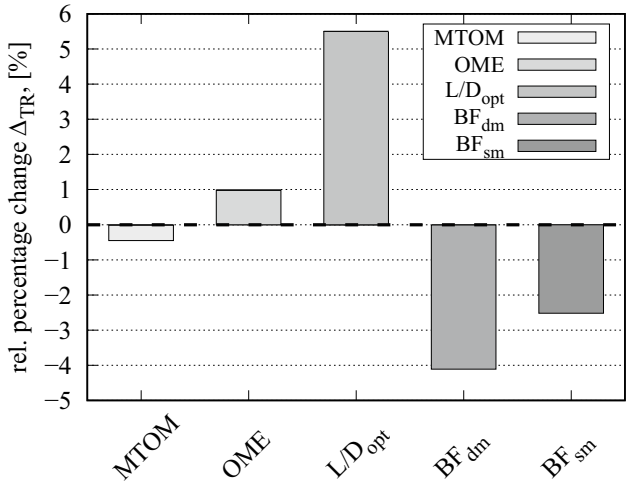

Fig. 16 Rel. percentage change compared to TR

the maximum possible laminarity from Fig. 7 and the respective local lift coefficients, it can be stated that the potential is almost completely exhausted by optimizing the suction distribution. Especially the cross-flow instabilities are suppressed until the end of the suction area and do not lead directly to flow transition. To increase the laminar area even further, therefore, either the wing planform or the 2D airfoil geometries must be adapted and optimized.

Nevertheless, the laminarity leads to a considerable shift of the drag polars of the wing; this shift is shown in Fig. 15.

It is obvious that the integration of an HLFC system and the resulting laminar area on the wing shifts the turbulent drag polar to significantly lower drag coefficients. For example, for $C_L = 0.5$, a reduction of more than 16 drag counts (dc) is achieved. For the retrofit design, the aerodynamic data resulting from the integration of HLFC are fed back into the design loop and the masses of individual components are recalculated until convergence. This allows a conclusion about the difference between the turbulent and the laminar configuration. This explicitly does not involve any geometric changes to the turbulent reference configuration, making the HLFC system an "add-on" to the existing design. Based on these results, an HLFC-optimized retrofit design of the ARB2028 can be designed with MICADO taking the following points into account:

- Geometrically unchanged ARB2028;
- Krueger flaps;
- Mass increase due to HLFC system and resizing of individual system components;
- Decreased engine performance due to additional power offtakes;
- Aerodynamic benefit due to flow control.

The relative percentage changes compared to the TR are illustrated in Fig. 16 for the relevant key parameters from Table 6.

It is evident that the OME slightly increases by 1%; this is mainly due to the increased complexity of the high-lift devices at the leading edge and the additional HLFC system mass. The aerodynamic performance, however, significantly increases by about 5.5%, which reflects the polar shift in Fig. 15. This results in a reduction of the blockfuel necessary for the design mission (BF_{dm}) by approx. 4%; the blockfuel required for the study mission (BF_{sm}) is decreased by about 2.5%. The greater percentage saving for the design mission can be attributed to the longer cruise phase in which the HLFC system is operated. In addition, the reduction of the necessary BF_{dm} outweighs the increase of the OME and thus leads to a reduction of the MTOM by about 0.5%.

To conclude, the optimized HLFC retrofit design reveals promising savings potential. Nevertheless, the next section examines the actual benefits of the optimization studies. Based on these results, design guidelines for future HLFC retrofit designs will be derived.

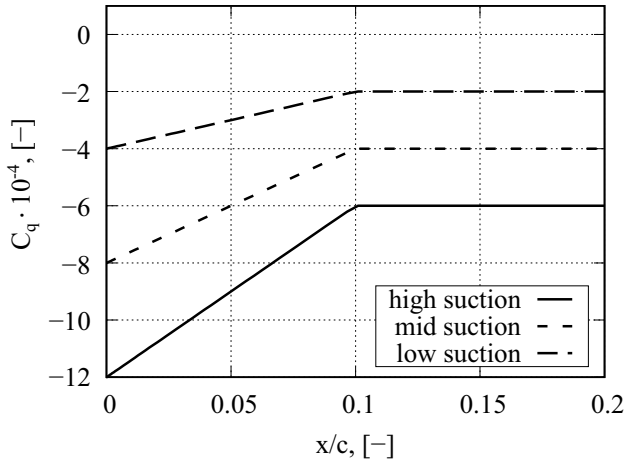

Fig. 17 Different suction distributions for investigation

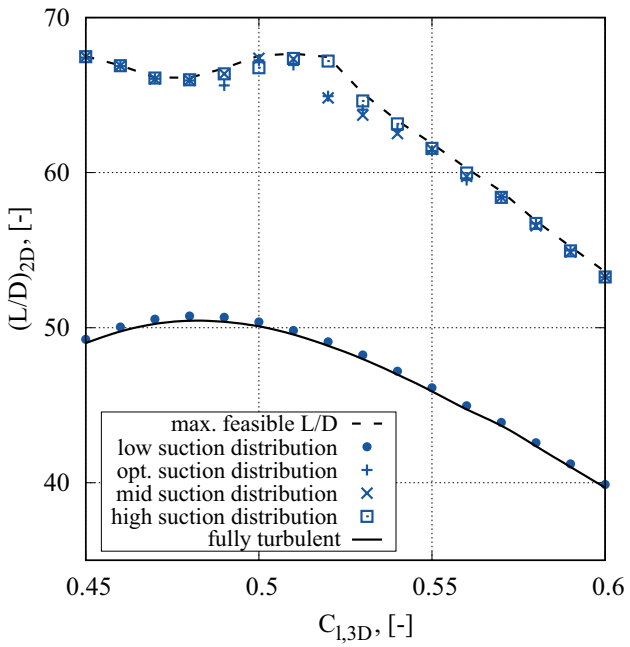

Fig. 18 Aerodynamic performance for four different suction distributions at $\eta = 0.32$

5 Examination of actual benefit

To investigate the actual impact of the optimization on the final design, additional databases for three, non-optimized suction distributions are set up. These distributions, which are kept constant along the span, are shown in Fig. 17.

For the additional suction distributions, the boundaries from Sect. 4 are maintained, i.e., $(x/c)_{\text{sec2,start}} = 0.1$ and $(x/c)_{\text{suction,end}} = 0.2$, respectively. The aerodynamic performance for these four suction distributions is shown

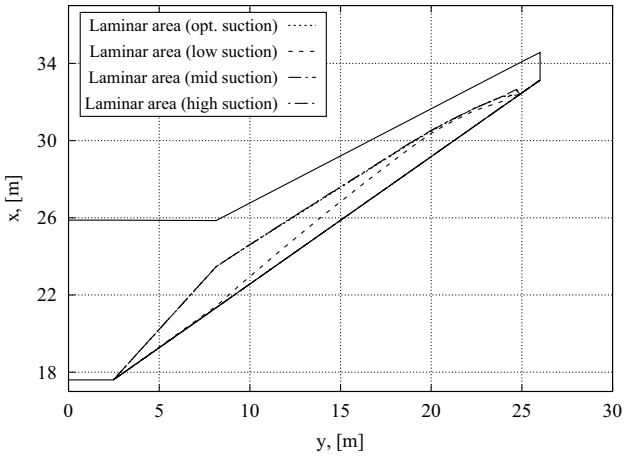

Fig. 19 Influence of different suction distributions on laminar area

exemplary for $\eta = 0.32$ in Fig. 18 over a range of $0.45 \leq C_l \leq 0.6$; the results from the other sections at $\eta = 0.77$ and $\eta = 0.95$ can be found Figs. 24 and 25 in the Appendix. In addition, the lower limit (fully turbulent flow) and the upper limit (maximum performance) of the studies from Sect. 4.1 are highlighted again.

As can be seen in Fig. 18, the low suction strength (blue dots) is not sufficient to suppress the cross-flow vortices at present Reynolds numbers and the local leading-edge angle. As a result, an almost completely turbulent flow is present. Analogous to the suction identified as optimal, the other two additional suction strengths in turn move close to the upper limit; therefore, the aerodynamic effects are estimated to be low at this wing section. It is noticeable, however, that the aerodynamic performance with the optimal suction distribution is below that with the high suction strength between $0.51 \leq C_l \leq 0.54$. This indicates that both are within the tolerance range of the aerodynamic losses, and the final selection in Sect. 4.1 was based on the necessary mass flow.

The resulting laminar areas for the respective optimum point of every suction distribution are shown in Fig. 19.

Although four different suction strengths are used, only two different laminar areas can be identified. This reflects the initial estimation of the aerodynamic performance at the kink in Fig. 18: While the performance is close to the maximum for the mid, the optimized, and the high suction strength, the low suction strength is not sufficient to suppress the cross-flow instabilities at this position. Only in the outer wing area, a laminar flow is achieved, since the cross-flows are less amplified due to the tapering of the wing and thus lower chord Reynolds numbers [8]. In addition, differences in the respective C_p-distributions influence the amplification of CFI. In this case, a smaller suction peak at $\eta = 0.77$ compared to $\eta = 0.32$ and $\eta = 0.95$, as can be seen, e.g., in Fig. 5, prevents a strong amplification of cross-flows. Due to these two effects, the instabilities can, therefore, be suppressed

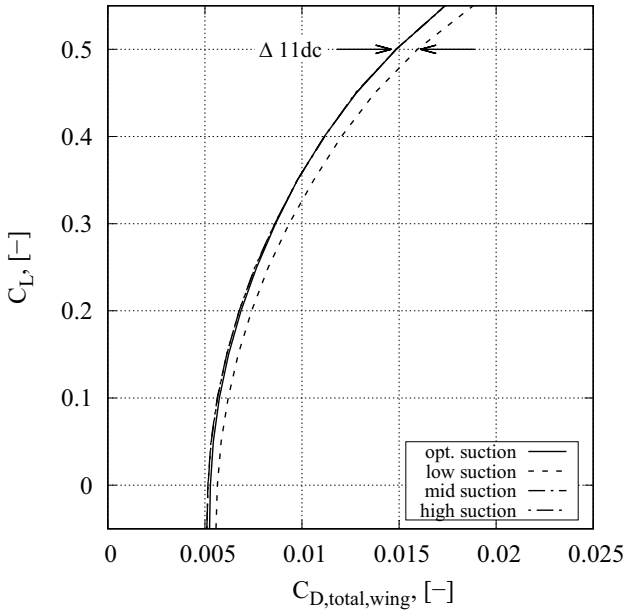

Fig. 20 Influence of different suction distributions on wing polars

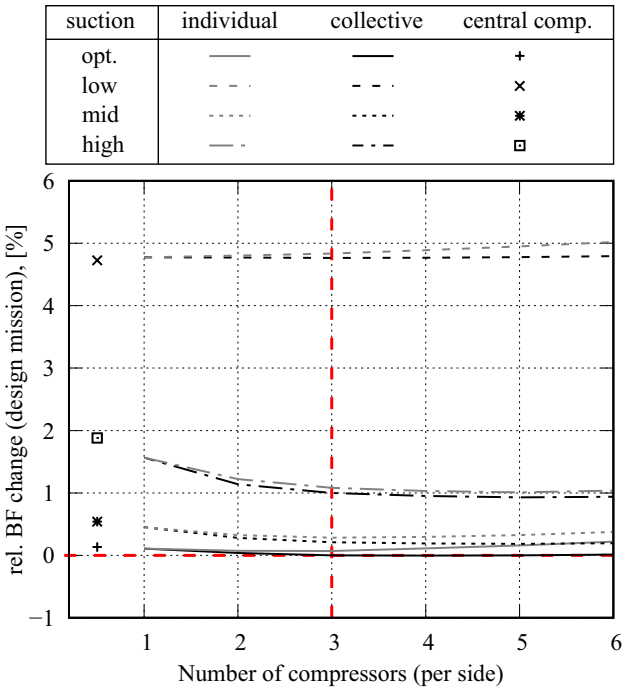

Fig. 21 Rel. BF change for varying suction distributions and HLFC system architectures

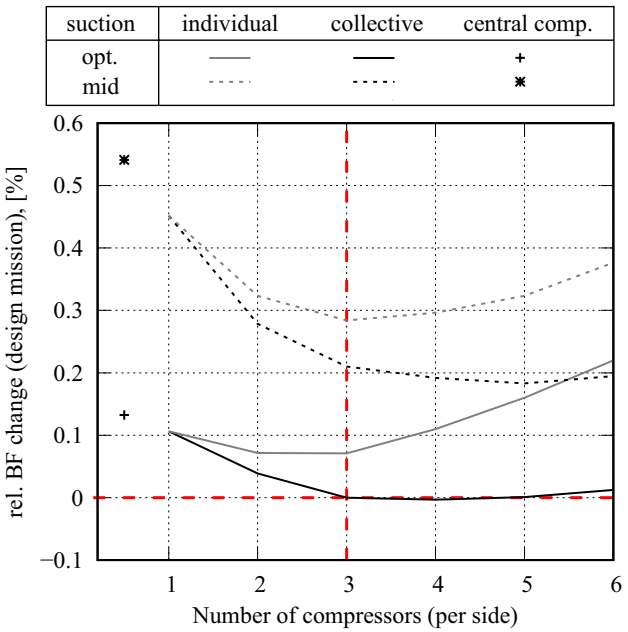

Fig. 22 Rel. BF change for mid and opt. suction strengths and various system architectures (enlarged)

even with low suction. The findings can also be seen in the wing polars in Fig. 20.

Here, likewise, only the polar curve resulting from the low suction strength is delimited. Therefore, it can be noted that only a too low suction strength, which cannot prevent a transition of the flow in the leading edge area, leads to significant losses in aerodynamic performance (e.g., $\Delta C_{D@C_L=0.5}$ ≈11 dc). In contrast, the slight deviations of the aerodynamic performances for the different suction strengths in Figs. 18, 24, and 25 lead to negligible effects on the laminar area and thus on the total drag polars of the wing.

To investigate not only the actual benefit of the optimized suction strengths but also the benefit of the optimized HLFC system architecture, a final study is conducted on OAD level. For this, the HLFC retrofit is redesigned for the additional three suction distributions; furthermore, the influence of the different HLFC system architectures in terms of ducting and number of compressors is analyzed. The results of this study are presented in Fig. 21 by the relative blockfuel change for the design mission compared with the optimized HLFC retrofit design from Sect. 4.

It becomes clear that in none of the variants examined an individual ducting architecture (gray curves) is favorable. In addition, it is evident that the reduced laminar area for the low suction strength in Fig. 19 increases the overall blockfuel consumption by at least about 4.75% for each HLFC system architecture investigated. Although the aerodynamics increase due to the laminar area on the OB wing, the additional masses and power offtakes eliminate this benefit, so the final design even increases the BF consumption of the turbulent ARB2028 (see Fig. 16). Furthermore, the version with the high suction strength also leads to considerable losses in efficiency gains; this is mainly due to the greatly increased HLFC system mass and power offtakes. The differences between the mid and the optimized suction,

however, are almost not recognizable within Fig. 21. Thus, an enlarged version of the respective interval is provided in Fig. 22.

In this enlarged illustration, two things can be pointed out: On the one hand, the approach of choosing an HLFC system architecture solely based of mass, power offtakes, and their respective gradients is sufficient, since this architecture (marked in red) could hardly be further optimized by a study at OAD level. On the other hand, however, the differences between the two suction strengths shown and the system architectures remain almost negligible; this applies in particular for the expected accuracy in preliminary aircraft design. Thus, the following design guidelines for future HLFC retrofit designs can be derived:

- It is essential to avoid using a suction system that is not strong enough to prevent an early transition;
- Only if the highest possible optimization accuracy from OAD perspective is desired, a more extensive approach for the selection of the suction distribution is recommended; for this, the study parameters from Table 4 and the approach presented in Fig. 10 can be used;
- For the HLFC system, it is favorable to use a collective ducting architecture;
- The investigated parameters of the HLFC system architecture have a minor influence on final key parameters such as blockfuel; thus, the selection of an architecture prior to the actual design is sufficient;
- The number of compressors used is not defined by the influence on blockfuel; instead, in the future, more attention can be paid to requirements from wing design (such as installation space) and cost-efficiency.

6 Conclusion

In the presented research, an approach for an optimized HLFC retrofit design was presented. To achieve the highest possible aerodynamic accuracy, known limitations of the methods used were successfully eliminated using synergy effects from the consortium; in particular, pressure distributions from a 2D flow solver were approximated to high fidelity TAU results. Furthermore, the suction distributions at specific wing sections and the HLFC system architecture were optimized; the results were subsequently used to derive an HLFC retrofit design. This design exploits the potential for hybrid laminar flow control as an add-on to an existing turbulent reference design. Promising blockfuel reduction potential could be identified with more than 4% savings for the design mission over 4600 NM compared to the turbulent reference. The extended studies in Sect. 5, however, indicated that the conducted optimization could only slightly increase the final savings potential. Therefore, in addition to the derived design guidelines for future retrofit designs, it is concluded that the full potential of HLFC technology should not be demonstrated by means of a retrofit design, but only by a wing designed with possible laminarization as a requirement. The new wing design methodology required for this, which uses more aerodynamic information as well as an airfoil selection process, is a current research topic at ILR and will be further developed in the course of the AVACON project. Nonetheless, it has to be emphasized that the presented approach of improving the aerodynamic accuracy was only feasible thanks to an already existing RANS computation performed on the whole wing. To improve the accuracy of the 2D computations already in an early stage of aircraft design, however, new solutions must be found that are not based on time-consuming 3D calculations. For this, a new project has been initiated in which multiple TAU computations lead to the derivation of reduced-order models. These can either replace the current 2D solver or calibrate its results. This would eliminate the need to improve the aerodynamic accuracy prior to the actual aircraft design and accelerates the presented approach to derive an optimized laminar (retrofit) aircraft design.

Appendix A

See Figs. 23, 24 and 25.

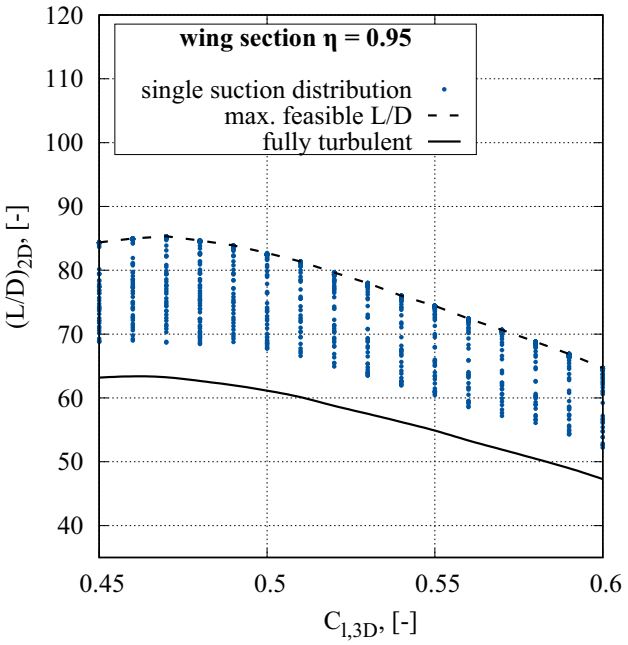

Fig. 23 Aerodynamic performance increase for different suction distributions ($\eta = 0.95$)

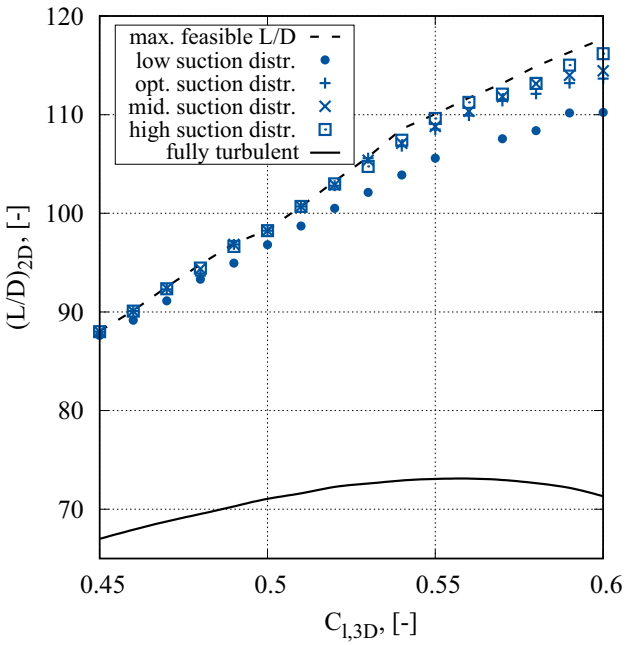

Fig. 24 Aerodynamic performance for four different suction distributions at $\eta = 0.77$

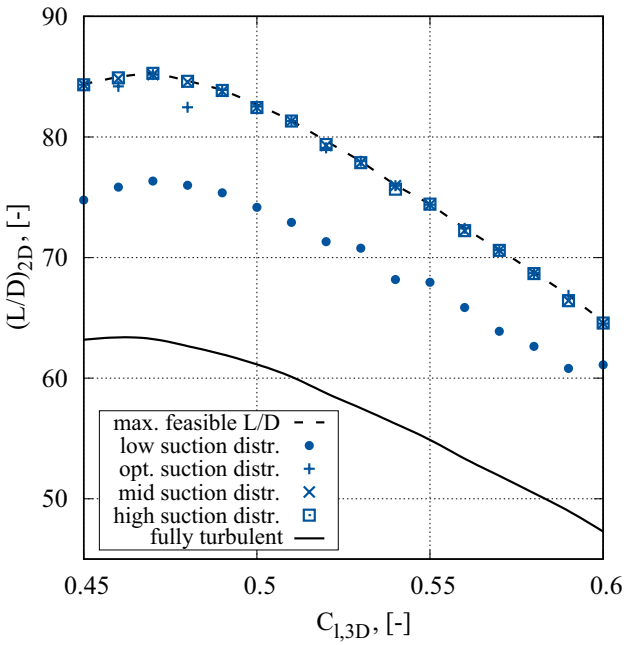

Fig. 25 Aerodynamic performance for four different suction distributions at $\eta = 0.95$

Acknowledgements The research presented in this publication has been conducted within the framework of the AVACON (Advanced Aircraft Concepts) project and has received funding from the German national research program *Luftfahrtforschungsprogramm V.3*. The authors would like to acknowledge both the support of the *Bundesministerium für Wirtschaft und Energie* (BMWi) and the project partners from DLR-AS for their contribution and valuable discussions.

Funding Open Access funding enabled and organized by Projekt DEAL.

References

1. Anderson, J.D.: Introduction to Flight, 8th edn. McGraw-Hill Education, New York (2016)
2. Arnal, D., Archambaud, J.P.: Laminar-Turbulent Transition Control: NLF, LFC, HLFC. Rhode St. Genesé (2008)
3. Boppe, C.: Aircraft Drag Analysis Methods. In: North Atlantic Treaty Organization (ed.) Special Course on Engineering Methods in Aerodynamic Analysis and Design of Aircraft, vol. AGARD-R-783, pp. 7.1–7.50. Neuilly-sur-Seine, France (1992)
4. Busemann, A.: Aerodynamischer Auftrieb bei Über-schallgeschwindigkeit. In: Reale Accademia d'Italia (ed.) 5th Volta Conference, Rome (1935)
5. Drela, M., Youngren, H.: XFOIL 6.99 User Guide. Tech. Rep. [user guide]. Massachusetts Institute of Technology, Cambridge (2013)
6. Drela, M.: A User's Guide to MSES 3.05. Tech. Rep. [user guide]. Massachusetts Institute of Technology, Cambridge (2007)
7. Drela, M.: XFOIL: An Analysis and Design System for Low Reynolds Number Airfoils. In: Mueller, T.J. (ed.) Low Reynolds Number Aerodynamics. Lecture Notes in Engineering, vol. 54. Springer, Berlin (1989)
8. Effing, T., Schültke, F., Stumpf, E.: Investigation of the influence of the Reynolds number on the prediction accuracy of laminar drag components. In: DGLR (ed.) 67. Deutscher Luft- und Raumfahrtkongress, Friedrichshafen (2018)
9. Flightpath 2050.: Europe's Vision for Aviation. Publications Office of the European Union, Luxembourg (2011)
10. Hood, R.V., Middleton, D.B., Hanks, G.W., Moyer, A.E., Ledbetter, G.E., Nagel, A.L., et al.: Hybrid Laminar Flow Control Study. Tech. Rep. NASA/CR-165930, NASA Langley Research Center, Hampton (1982)
11. Horstmann, K.H., Engelbrecht, T., Liersch, C.M.: LIFTING_LINE v3.0 Handbook. Tech. Rep. [user guide], DLR Institute of Aerodynamics and Flow Technology, Braunschweig (2019)
12. Horstmann, K.H., Schrauf, G., Sawyers, D.M., Sturm, H.: A Simplified Suction System for an HLFC Leading Edge Box of an A320 Fin. In: Council of European Aerospace Societies (ed.) CEAS Aerospace Aerodynamics Research Conference. CEAS, Cambridge (2002)
13. Horstmann, K.H.: Ein Mehrfach-Traglinienverfahren und seine Verwendung für Entwurf und Nachrechnung nichtplanarer Flügelanordnungen. Tech. Rep. FB 87-51, German Test and Research Institute for Aviation and Space Flight (DFVLR), Braunschweig (1987)

14. Iannelli, P., Wild, J., Minervino, M., Strüber, H., Moens, F., Vervliet, A.: Design of a high-lift system for a laminar wing. In: EUCASS Association (ed.) 5th European Conference for Aeronautics and Space Sciences (2013)
15. Joslin, R.D.: Overview of Laminar Flow Control. Tech. Rep. NASA/TP-1998-208705, NASA Langley Research Center, Hampton (1998)
16. Lange, F.: High fidelity design of the AVACON research baseline aircraft based on CPACS data set. In: 54th 3AF International Conference on Applied Aerodynamics, Paris (2019)
17. Lock, R.: An Equivalence Law Relating Three- and Two-Dimensional Pressure Distributions. Tech. Rep. Vol. 3346, H.M. Stationery Office, London (1962)
18. Pe, T., Thielecke, F.: Synthesis and Topology Study of HLFC System Architectures in Preliminary Aircraft Design. In: Council of European Aerospace Societies (ed.) 3rd CEAS Air & Space Conference, Venice (2011)
19. Pe, T.: HLFC Technology Integration and Assessment. Tech. Rep. FST-PB-2013-32 (final report for LuFo projects HIGHER-LE and VER^{2}SUS), Hamburg University of Technology, Hamburg (2013)
20. Pfenninger, W.: Laminar flow control–laminarization. In: Special Course on Concepts for Drag Reduction, vol. AGARD-R-654, pp. 3.1–3.75 (1977)
21. Pohya, A.: Selected current challenges in the development of hybrid laminar flow control on transport aircraft. In: DGLR (ed.) 68. Deutscher Luft- und Raumfahrtkongress, Darmstadt (2019)
22. Poll, D.: Transition in the infinite swept attachment line boundary layer. Aeronaut. Q. **30**, 607–629 (1979)
23. Redeker, G., Wichmann, G.: Laminarhaltung an ungepfeilten und gepfeilten Flügeln. Tech. Rep. AD 02 02 005, DLR Institute of Aerodynamics and Flow Technology, Braunschweig (1995)
24. Reed, H.L., Saric, W.S.: Stability of three-dimensional boundary layers. Annu. Rev. Fluid Mech. **21**(1), 235–284 (1989)
25. Reneaux, J., Preist, J., Juillen, J., Arnal, D.: Control of attachment line contamination. In: Council of European Aerospace Societies (ed.) 2nd European Forum on Laminar Flow Technology. CEAS, Bordeaux (1996)
26. Risse, K., Anton, E., Lammering, T., Franz, K., Hoernschemeyer, R.: An integrated environment for preliminary aircraft design and optimization. In: American Institute of Aeronautics and Astronautics (ed.) 53rd AIAA/ASME/ASCE/AHS/ASC Structures, Structural Dynamics and Materials Conference: SciTech 2012, vol. 2012-1675. AIAA (2012)
27. Risse, K.: Preliminary Overall Aircraft Design with Hybrid Laminar Flow Control. Ph.D. thesis, RWTH Aachen University, Aachen (2016)
28. Rossow, C.C.: Aerodynamics—a discipline swept away? Aeronaut. J. **114**(1160), 599–609 (2010)
29. Schlichting, H., Gersten, K.: Grenzschicht-Theorie, 10th edn. Springer, Berlin (2006)
30. Schrauf, G., von Geyr, H.: Simplified hybrid laminar flow control for the A320 Fin: aerodynamic and system design, first results. In: American Institute of Aeronautics and Astronautics (ed.) AIAA Scitech 2020 Forum. Orlando (2020)
31. Schrauf, G.: COCO: A Program to Compute Velocity and Temperature Profiles for Local and Nonlocal Stability Analysis of Compressible. Conical Boundary Layers with Suction. Tech. Rep. ZARM, Airbus, Bremen (1998)
32. Schrauf, G.: LILO 2.1: User's Guide and Tutorial. Tech. Rep. GSSC 6, Airbus, Bremen (2006)
33. Schrauf, G.: Status and perspectives of laminar flow. Aeronaut. J. **109**(1102), 639–644 (2005)
34. Schültke, F., Aigner, B., Effing, T., Strathoff, P., Stumpf, E.: MICADO: overview of recent developments within the conceptual aircraft design and optimization environment. In: DGLR (ed.) 69. Deutscher Luft- und Raumfahrtkongress, Aachen (2020)
35. Schültke, F.: Methodik zur Auslegung von Flügeln mit Hybridlaminarisierung im Flugzeugvorentwurf. Master thesis, RWTH Aachen University, Aachen (2013)
36. Schültke, F., Stumpf, E.: Cross-flow effects regarding laminar flow control within conceptual aircraft design. Aircr. Eng. Aerosp. Technol. **89**(4), 620–631 (2017)
37. Schwamborn, D., Gerhold, T., Heinrich, R.: The DLR TAU-code: recent applications in research and industry. In: European Conference on Computational Fluid Dynamics, Egmond aan Zee (2006)
38. Streit, T., Wichmann, G., von Knoblauch zu Hatzbach, F., Campbell, R.L.: Implications of Conical Flow for Laminar Wing Design and Analysis. In: American Institute of Aeronautics and Astronautics (ed.) 29th AIAA Applied Aerodynamics Conference, Honolulu (2011)
39. Torenbeek, E.: Synthesis of Subsonic Airplane Design. Kluwer Academic Publishers, Dordrecht (1982)
40. Vassberg, J.C., DeHaan, M.A., Rivers, S.M., Wahls, R.A.: Development of a common research model for applied CFD validation studies. In: American Institute of Aeronautics and Astronautics (ed.) 26th AIAA Applied Aerodynamics Conference, Honolulu, vol. 2008-6919, pp. 1–22 (2008)
41. Wicke, K., Linke, F., Gollnick, V., Kruse, M.: Insect contamination impact on operational and economic effectiveness of natural-laminar-flow aircraft. J. Aircr. **53**(1), 158–167 (2016)
42. Woehler, S., Hartmann, J., Prenzel, E., Kwik, H.: Preliminary aircraft design for a midrange reference aircraft taking advanced technologies into account as part of the AVACON project for an entry into service in 2028. In: DGLR (ed.) 67. Deutscher Luft- und Raumfahrtkongress, Friedrichshafen (2018)
43. Young, T.M.: Investigations into the Operational Effectiveness of Hybrid Laminar Flow Control Aircraft. Ph.D. thesis, Cranfield University, Cranfield (2002)
44. Young, T.M., Humphreys, B.: Liquid anti-contamination systems for hybrid laminar flow control aircraft—a review of the critical issues and important experimental results. Proc. Inst. Mech. Eng. Part G J. Aerosp. Eng. **218**, 267–277 (2004)